UC Berkeley
UC Berkeley Previously Published Works

Title

Back-to-back high category atmospheric river landfalls occur more often on the west coast of the United States

Permalink

https://escholarship.org/uc/item/3vn3n0c1

Journal

Communications Earth & Environment, 5(1)

ISSN

2662-4435

Authors

Zhou, Yang

Wehner, Michael

Collins, William

Publication Date

2024

DOI

10.1038/s43247-024-01368-w

Copyright Information

Peer reviewed

Back-to-back high category atmospheric river landfalls occur more often on the west coast of the United States

Check for updates

Yang Zhou [1] ✉, Michael Wehner [2] & William Collins [1,3]

The catastrophic December 2022-January 2023 nine atmospheric rivers in California underscore the urgent need to better understand such high-risk weather extremes. Here we applied a machine learning clustering tool to understand the activity of atmospheric river clusters. Reanalysis results show that clusters with high density, that is the time fraction under atmospheric river conditions within a cluster, exhibit more frequent high-category atmospheric rivers, alongside an increased likelihood for extreme precipitation and severe land surface responses. The key circulation patterns of atmospheric river clusters are primarily attributed to subseasonal variability. Furthermore, the occurrence and density of atmospheric river clusters are modulated by the daily variability of the geopotential height field. Climate model projections suggest that atmospheric river clusters with higher density and higher categories will be more frequent as warming level increases. Our findings emphasize the important role of atmospheric river clusters in the development of climate adaptation and resilience strategies.

From late December 2022 to mid-January 2023, California experienced a series of nine atmospheric rivers (ARs) making landfall. This compounding weather event led to devastating consequences, including severe flooding and landslides, widespread power outages, and at least 22 fatalities[1]. An "AR cluster", i.e., spatiotemporally compounding ARs, is defined as multiple AR landfalls over a region within a short period. Past studies have revealed that the precondition of the land surface, including antecedent soil moisture and existing snowpack, can lead to a higher runoff-to-precipitation ratio during ARs[2–5]. When an AR cluster occurs, there may not be sufficient time for the soil moisture and other land properties to recover between events, which potentially precondition the soil for higher flood risk. However, there have been only a few studies that focus on understanding the activity and projection of AR clusters. Fish, Wilson[6] defined the term "AR families" for the length of time in which multiple ARs make landfall and analyzed the associated semi-stationary synoptic patterns, which are partially modulated by El Nino Southern Oscillation[7]. A recent study focuses on the subseasonal clustering of ARs over the western U.S. and demonstrates the regional difference in cluster counts[8]. These studies highlight the AR cluster's contribution to coastal extreme precipitation. Although numerous previous studies indicate that ARs are projected to be more intense in the warmer climate[9–11], limited research has focused specifically on the future changes of temporal clustering ARs. It has been shown that the intensity and duration

of consecutive ARs increase with the increasing temperature[12]. The more frequent back-to-back ARs result in unprecedented monthly precipitation total by end century[10]. Focusing on the 2017 Oroville Dam crisis, a study shows that the precipitation associated with the two consecutive ARs would increase by up to 21-59% under the late-21st century scenario[13]. That being noted, limited work suggests that precipitation from ARs associated with an extratropical cyclone respond strongly to global warming while those without an extratropical cyclone do not[14].

Motivated by the significant impacts of the 2023 nine-AR series[15], our research aims to advance the current understanding of AR clusters by evaluating variations in their characteristics, circulation patterns, and impact levels. We hypothesize that AR clusters have diverse characteristics and landfall impacts, influenced by variations in landfall duration, spacing between landfall events, and event intensity. Here, we build on previous work by incorporating unique analysis techniques such as cluster density and future projections. In this work, we utilize a data-driven unsupervised machine learning algorithm to identify landfalling AR clusters over the U.S. West Coast. We compare AR clusters with different densities of landfall occurrences and find that AR clusters have substantial impacts when landfalls are densely distributed. We find that high-category AR events are more prone to occur as back-to-back ARs, with an associated high flood risk. We identify the key circulation pattern associated with AR cluster activity.

[1]Climate and Ecosystem Sciences Division, Lawrence Berkeley National Laboratory, Berkeley, CA, USA. [2]Applied Mathematics and Computational Research Division, Lawrence Berkeley National Laboratory, Berkeley, CA, USA. [3]University of California, Berkeley, CA, USA. ✉e-mail: yzhou2@lbl.gov
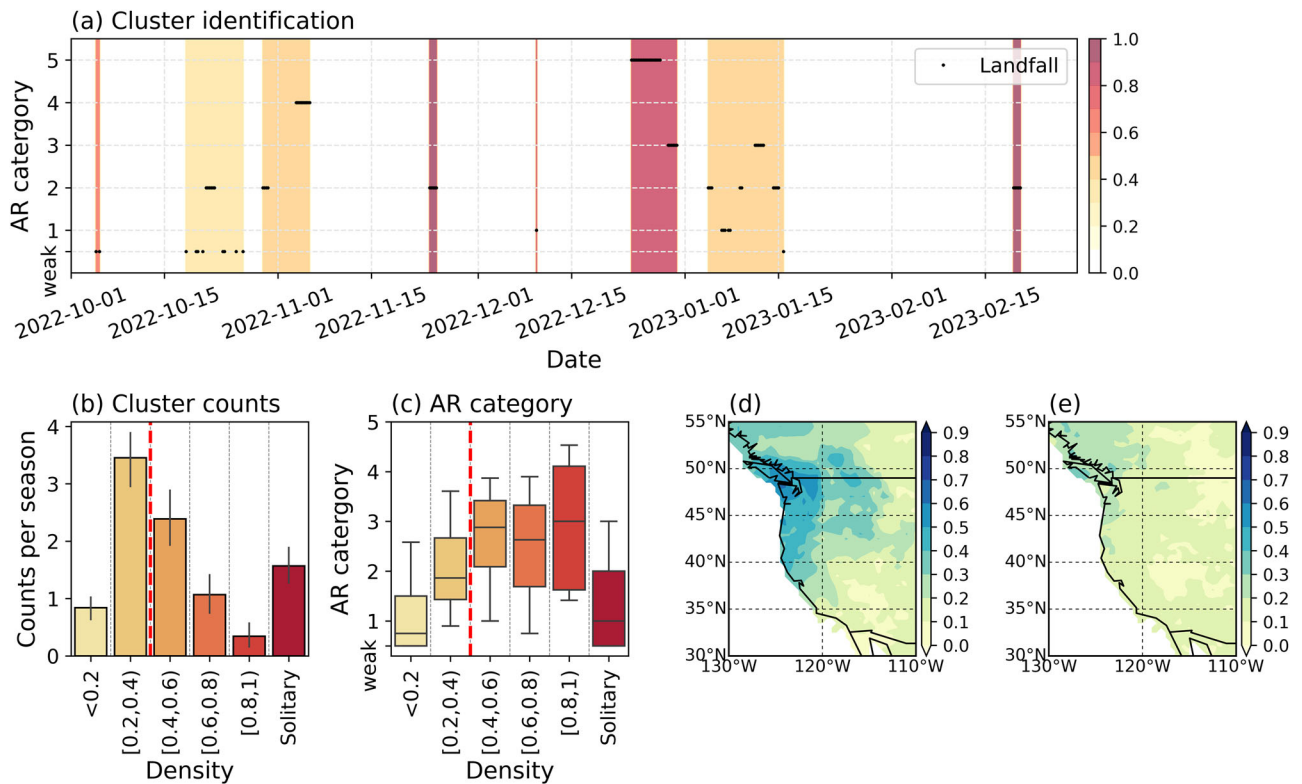
Fig. 1 | Identification of atmospheric river (AR) clusters and AR cluster characteristics based on cluster density. a An example that shows the identification of AR clusters from October 2022 to February 2023 calculated from ERA5 reanalysis data. Please note that the focused period in other years is from October to April. Y-axis denotes the category of the landfalling ARs. The black dots/lines mark both the time steps and the scaling of ARs making landfall over the U.S. West Coast. The filled background represents the time periods (with respect to the x-axis) identified as AR clusters. The filling color represents the density of an AR cluster, i.e., the percentage of AR conditions within a cluster. The comparisons based on cluster density are shown as boxplots for (**b**) cluster counts (unit: number per season) and (**c**) averaged AR category within a cluster. The red dashed line denotes the partition of dense clusters and sparse clusters based on the 50th percentile of cluster density. For (**b**), the vertical line denote the 95% confidence interval. For (**c**), the center line marks the median value of the distribution. The two box ends represent the first and third quartiles of data. The whiskers extend from the box to the 5th and 95th percentile of data. Spatial maps showing the fraction of AR-related extreme precipitation days to total extreme precipitation days of (**d**) dense clusters and (**e**) sparse clusters. Extreme precipitation is defined as grid-point precipitation exceeding the 98th percentile of the record of 44 cool seasons. We extend the upper boundary to 55°N because part of British Columbia is also influenced by AR clusters over the U.S. West Coast.

Moreover, the density of AR clusters is projected to slightly increase in future climates, along with increasing AR category[10]. This study underscores the importance of understanding the characteristics and variability of AR clusters to enhance the adaptation and preparedness for flood risk and to restore resilience for both natural and built environments.

Results
Characteristics of AR clusters
One of the challenges in AR cluster analysis is the identification of AR clusters. Past studies either used a count-based approach to combine individual events that occur within a fixed period[6,7] or applied moving average to identify successive periods of integrated vapor transport[12]. However, AR occurrence within a fixed period may emphasize event occurrence but overlook the AR landfall duration which is an important factor for soil precondition. Also, stronger ARs possess higher weights in the moving-average process. Besides, the aggregation period for AR clusters is regional-dependent[8], which means that the windows for a cluster to happen greater than random chance varies by location. We applied a data-driven clustering algorithm called "Mean Shift" to identify AR clusters that consist of single or multiple AR landfalls (details in Methods). This algorithm automatically identifies temporal clusters from the generated time series of AR landfall flags, which is a great tool to help us investigate AR clusters' variability and associated circulation patterns.

We mark clusters with only one AR landfall as "solitary clusters", which means the spacing between this event and other landfalls is so large that the

algorithm identifies itself as a cluster. The identified AR clusters in the 2022-2023 cool season are shown as an example (Fig. 1a). The 2023 nine AR series is grouped into two clusters with one cluster in late December 2022 containing a Category 5 and a Category 3 AR (AR scaling based on Ralph, Rutz[16]), and one cluster covering early January 2023 with seven ARs with categories from Weak to Category 3.

The AR clusters contain "AR days", the days within an AR landfall, and "non-AR days", the days between storms. We define the density of an AR cluster by, for each cluster, the ratio of the number of AR days and the total number of cluster days. For solitary clusters, the cluster density will be 1. Excluding solitary clusters, we divide the AR clusters into two groups based on the 50th percentile of cluster density: dense clusters (≥ 50th percentile) and sparse clusters (<50th percentile). The dense clusters are more active from October to January, with the peak occurrence in November (Supplementary Fig. 1a). Sparse clusters are active throughout the season with a slight decrease after February. The solitary clusters mostly appear after January. The temporal distribution of AR activity agrees with previous findings[17]. During the boreal cold season, dense clusters show higher AR frequency (calculated as percent of AR condition time steps) over the U.S. West Coast compared to sparse clusters, which is likely due to fewer non-AR time steps included in the dense clusters. Especially, the AR frequency in dense clusters is 100-150% higher than that in sparse clusters along the U.S. West Coast between 35° and 50°N. Also, ARs in dense clusters extend further inland and reach approximately 117°W (Supplementary Fig. 1b, c).
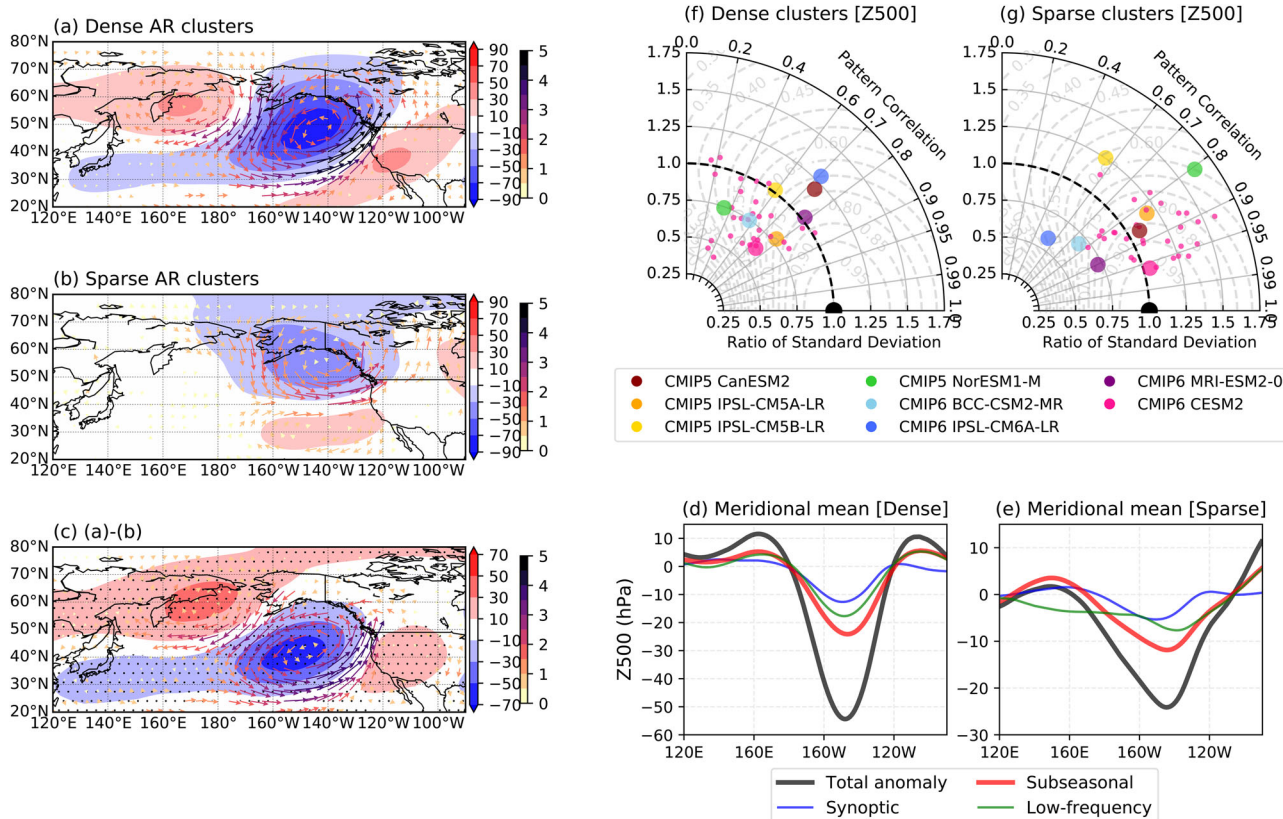
Fig. 2 | Large-scale circulation patterns associated with atmospheric river (AR) cluster. Composite maps of daily anomalous 500 hPa geopotential height (Z500, unit: m) and daily anomalous 850 hPa wind (unit: m s^{-1}) during (**a**) dense clusters, (**b**) sparse clusters, (**c**) the difference between dense and sparse clusters. The meridional mean of Z500 anomalies between 20°N–70°N for (**d**) dense clusters and (**e**) sparse clusters. The Z500 anomalies are decomposed into three temporal frequencies: synoptic (<20 days), sub-seasonal (20–100 days), and low-frequency (>100 days) using Lanczos filtering. Results in (**a**–**e**) are calculated using ERA5 reanalysis. Model comparison: Taylor diagrams showing the comparison of Z500 anomalous pattern in ERA5 reanalysis against models including CMIP5, CMIP6, and CESM2-LENS for (**f**) dense clusters and (**g**) sparse clusters.

The statistics of AR clusters vary by cluster densities. Excluding solitary events, the most frequent occurrence belongs to clusters with a density between 0.2 and 0.4. The occurrence frequency gradually decreases as density increases (Fig. 1b). Similarly, the size of clusters, which is defined as the time span of a cluster, decreases with density (Supplementary Fig. 2a). The size of solitary clusters represents the actual landfall duration of single events. Despite that sparse clusters last significantly longer than dense clusters, they both on average include 3–4 AR landfalls in a cluster (Supplementary Fig. 2b). The similarity in AR counts suggests that the cluster density is mainly attributed to the spacing between landfall events.

The average AR category of a cluster increases with increasing density (Fig. 1c). Higher-category ARs are more likely to occur closely packed in time. Along the U.S. West Coast, about 20-50% of the top 2% precipitation days happen during a dense cluster, and 10–20% of extreme precipitation days are in sparse clusters (Fig. 1d, e). Moreover, the mean precipitation intensity of dense clusters is significantly higher than that of sparse clusters (Supplementary Fig. 3). It is worth noting that more than 60-65% of the AR precipitation over the U.S. West Coast is attributed to dense AR clusters (not shown). Specifically, over Oregon and Washington, the AR precipitation intensity in dense clusters is 120–140% as strong as that for sparse clusters (Supplementary Fig. 3c). A similar pattern of AR clusters' contribution to extreme precipitation is shown with PRISM gridded observation (Supplementary Fig. 4).

The large distinction in AR precipitation by cluster densities results in variations in the associated landfall impacts (Supplementary Fig. 5). Both dense and sparse clusters can lead to near saturation of soil moisture in mountain ranges. Generally, sparse clusters induce a 10–40% increase in soil moisture saturation degree with a maximum over northern California, and

the dense clusters bring similar changes but in the range of a 20-50% increase. We show that runoff related to AR clusters contributes about 60% to total runoff along the U.S. coastal region (Supplementary Fig. 5k, l). While both cluster types increase runoff over the U.S. West Coast, the increased runoff by dense clusters is nearly 100% more than that by sparse clusters over northern California, and 150-300% more over the Cascade Range (Supplementary Fig. 5h–j).

Interaction between circulation and AR clusters

Previous studies have demonstrated that an intensified Aleutian Low boosts more landfalling ARs over the U.S. West Coast[18–20]. Our results indicate that such a connection varies by cluster density. Based on the composites of the 500 hPa geopotential height anomaly (Z500), there is a clear distinction in the circulation patterns associated with dense and sparse clusters (Fig. 2a-c). The dense clusters are linked to a Z500 pattern with tri-pole height anomaly centers over the North Pacific with a northwest-southeast orientation. The strong negative height anomaly system over the northeastern Pacific incites cyclonic flow. The southeast branch of the cyclonic flow has strong wind speed with a poleward direction, which is favorable for bringing moisture from the subtropics—the strong wind speed and rich moisture result in higher AR categories and greater landfall impacts. The Z500 pattern associated with sparse clusters shows a south-northward dipole pattern accompanied by a zonally-orientated eastward flow over the subtropical northeastern Pacific, which demonstrates spatial similarity with the 6th EOF pattern shown by Guirguis, Gershunov[20]. Our Z500 patterns also show agreement with Fish, Done[7] who applied k-means cluster analysis on Z500 associated with temporal clustering ARs. The Z500 pattern of dense clusters shows similarity to their "meridional patterns" which also contain positive
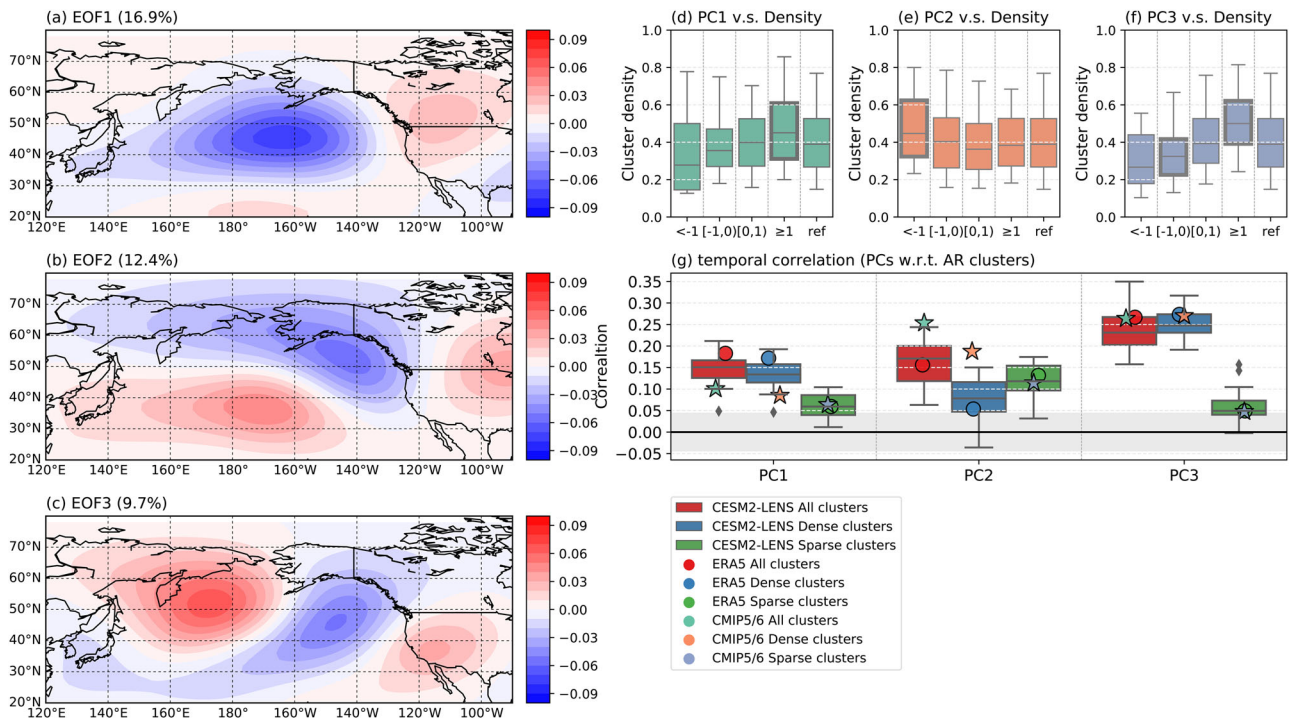
Fig. 3 | Connection between atmospheric river (AR) clusters and the daily variability of large-scale circulation. a–c The first three EOF modes of daily anomalous 500 hPa geopotential height were retrieved from ERA5 reanalysis. The percentage of variance explained is included in the subtitles. **d–f** Boxplots show how cluster density varies by principal components (PCs). The x-axis represents the normalized PC values, except for the last tick showing the reference distribution of AR cluster density. The center line marks the median value of the distribution. The two box ends represent the first and third quartile of data. The whiskers extend from the box to the 5th and 95th percentile of data. The distribution that is 90% significantly different from the reference (p value smaller than 0.1) is marked with thickened lines. **d–f** are calculated using ERA5 reanalysis. **g** Model comparison: correlation coefficients between the first three PCs and cluster indices of all AR clusters, dense clusters (50th percentile of total density) only, and sparse clusters (<50th percentile of total density) only. The AR cluster index is calculated as a binary time series, where a time step is marked as 1 if it is in an AR cluster, and it is masked as 0 otherwise. The colored dots mark the value from ERA5. The error bar shows the ensemble range of CESM2 and the colored stars are the mean of correlation coefficients from CMIP5/6 models.

Z500 anomaly upstream. The Z500 of sparse clusters is closer to their "zonal patterns" as the negative Z500 anomaly extends zonally[7]. We validate the key circulation pattern for dense and sparse clusters with model simulations (Fig. 2f-g). In general, the pattern of sparse clusters has a higher spatial correlation coefficient than that of dense clusters. One possible explanation is that the height pattern associated with dense clusters has more variability. Another possibility is that sparse clusters contain more non-AR days which can potentially smooth out the circulation signal associated with AR activity.

Given that ARs have close connections to climate variability of different time scales[18,21,22], we decompose the Z500 field into three time scales using Lanczos filtering[23]: synoptic (<20 days), subseasonal (20–100 days), and low-frequency (>100 days), to illustrate the dominant temporal frequency that modulates AR cluster activity. Results show that the subseasonal variation is the major contributor for both dense and sparse clusters, which explains about 40–50% of the total anomaly (Fig. 2d-e). The 2023 nine AR series, which are labeled as dense clusters, occurred during a decaying La Niña season. The Z500 of the 2023 nine AR series displays a La Niña teleconnection pattern with a weakened Aleutian Low and a strong positive height anomaly over the North Pacific (Supplementary Fig. 6a). Even though the La Niña teleconnection pattern generally discourages AR activity over the U.S. West Coast[17], the Z500 pattern during the 2023 nine AR series shows a statistically significant resemblance to the pattern for dense clusters when the low-frequency signal is removed (Supplementary Fig. 6b). A recent study focused on the 2023 nine AR series indicates that an active MJO was in phase when the AR cluster occurred[15].

We perform the Empirical Orthogonal Function (EOF) analysis on the daily Z500 field over the North Pacific between 20°N and 80°N to understand how AR clusters interact with circulation variability (Fig. 3a–c). The first EOF mode (EOF1) is significantly correlated, both temporally and

spatially with the Pacific-North America (PNA) pattern. The second EOF mode (EOF2) consists of tri-pole pressure centers over the North Pacific Ocean and North America, which shows a significant temporal correlation with climate variabilities including Western Pacific Oscillation[24] and Eastern Pacific Oscillation[25]. The EOF2 is similar to the key circulation pattern for sparse clusters (spatial correlation of 0.74), especially for the negative pressure center near Alaska. The third EOF mode (EOF3) shows tri-pole pressure centers over the North Pacific with a southwest-northeast orientation, almost identical to the key Z500 pattern for dense clusters (spatial correlation coefficient of 0.79). We do not include the fourth mode of EOF in the discussion because of its relatively lower correlation with AR clusters.

We then examine the connection between Z500 principal components (PCs) and AR clusters (Fig. 3d-f). Note that solitary clusters are excluded from the calculation. For PC1, higher cluster density appears for positive PC1s, meaning that dense AR clusters are more likely to coincide with a positive PNA pattern. This is consistent with previous analysis showing that increased AR frequency over the Pacific Northwest during positive PNA[26,27]. Meanwhile, higher cluster density corresponds to PC2 values that are smaller than −1. PC3 has the highest predictive power: cluster density increases as the PC3 value increases. Consistency is shown in the temporal correlation between AR cluster indices and PCs (Fig. 3g). The AR cluster index is a daily series with "0" and "1" flags showing whether a day is within an AR cluster. The AR cluster indices are generated with total AR cluster, dense AR cluster only, and sparse AR cluster only. The PC3 shows the highest temporal correlation with AR cluster indices which is mainly contributed by dense clusters. PC1 shows a positive correlation with AR clusters, which is also mainly attributed to dense clusters. Besides, the occurrence of positive PC2 is more coincidental with the occurrence of sparse clusters.
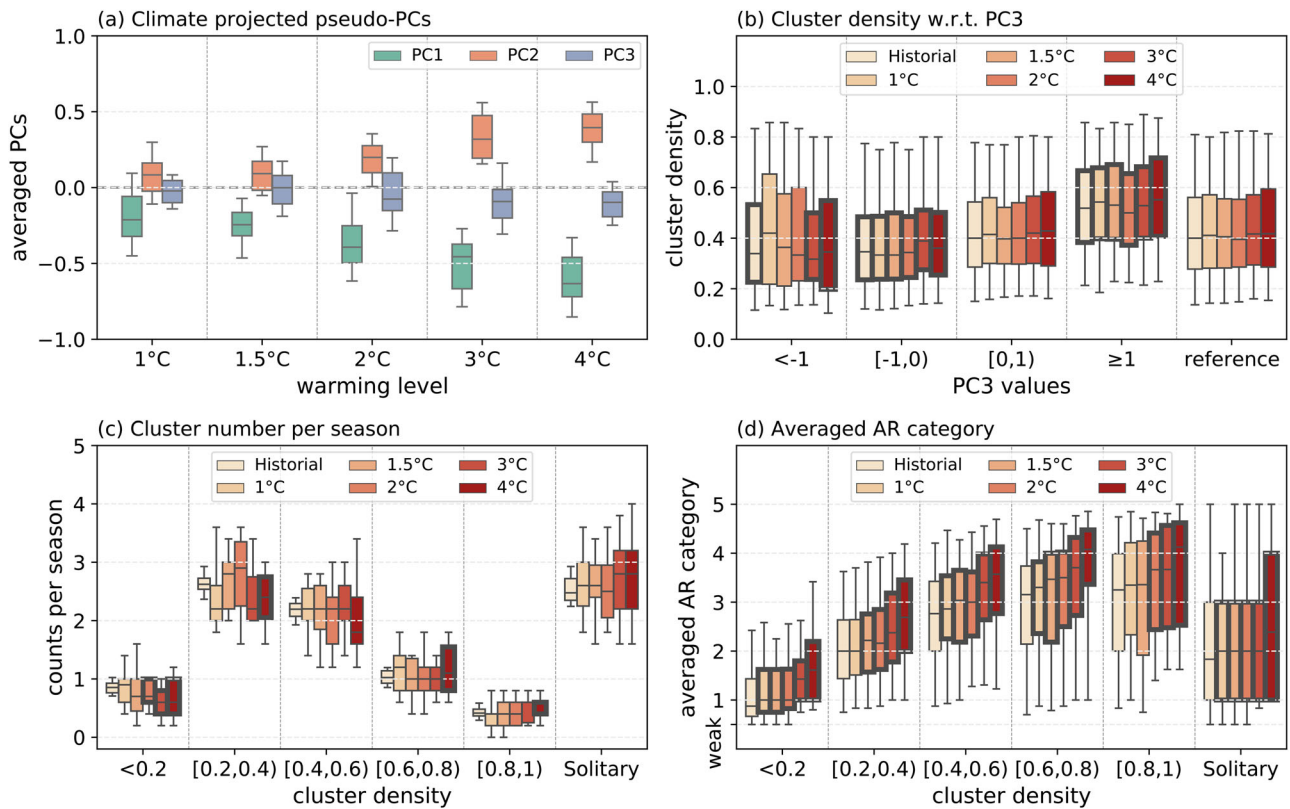
Fig. 4 | Changes of atmospheric river (AR) clusters in the warming climates.
a Averaged pseudo-PCs of CESM2-LENS SSP370 simulations on different warming levels. We show the first three modes of pseudo-PCs. The pseudo-PCs are calculated by projecting the EOFs of 500 hPa geopotential height (Z500) from CESM2-LENS historical simulation onto the SSP370 Z500 fields. For each warming level, five years are selected. The pseudo-PCs are first normalized based on historical PCs and then averaged through the 5 years. **b** Boxplot that shows how cluster density varies by the value of PC3 on different warming levels. The x-axis shows the normalized PC3 values except for the last tick which is the reference distribution of total cluster density. The distribution that, on the same warming level, is 90% significantly different from the reference (p value smaller than 0.1) is marked with thickened lines. Similar boxplots as (**b**) but are for (**c**) cluster number per season and (**d**) averaged AR category based on different groups of cluster density. In the boxplots, the center line marks the median value of the distribution. The two box ends represent the first and third quartile of data. The whiskers extend from the box to the 5th and 95th percentile of data. For each AR density group, the distribution that is 90% significantly different from the historical distribution (p value smaller than 0.1) is marked with a thickened line.

Most models show high consistency with ERA5 and capture the first three modes of variability. Although the agreement decreases for the second and third modes, the spatial correlations are mostly about 0.8 (Supplementary Fig. 7). In particular, models show higher agreement in reproducing the connection between EOF3 and AR clusters than the Z500 composite for dense clusters (Fig. 2f), suggesting that model bias may hinder the simulation of circulation patterns associated with dense cluster activity, but the connection between Z500 variability and AR clusters are well captured. For the temporal correlations between PCs and AR cluster indices, the models generally perform well. The correlations of ERA5 lie within the ensemble spread of CESM2-LENS. The multimodel mean from CMIP5 and CMIP6 models demonstrate consensus with reanalysis, especially for PC3.

AR clusters in warming climate
We show how the Z500 variability will change in future climates by projecting the CESM2-LENS historical EOFs onto its future simulations to generate pseudo-PCs that describe the occurrence frequency of EOF phases in the future climate. The historical daily mean is removed in future simulations before the projection. The pseudo-PCs are normalized using historical PC values to reflect the changes to historical simulations. We selected CESM2-LENS because the data is available for all warming levels, and contains 30 ensemble members for addressing uncertainty. Besides, CESM2-LENS shows the best skill in reproducing the patterns associated with cluster density (Fig. 2d–f) and Z500 EOF patterns (Supplementary Fig. 7). As the warming level increases, the averaged pseudo-PC1

continuously decreases, indicating that the opposite phase of EOF1 will emerge more often with increasing temperature. On the contrary, the pseudo-PC2 uniformly increases with increasing warming levels, which represents more frequent positive phases of the EOF2 in the future. This is consistent with previous studies that demonstrated a deepening and northward shifting of the Aleutian Low in future climate[28,29]. As for EOF3, the most relevant mode for dense AR clusters, no significant trend is displayed. The relation between PC3 and cluster density is reproduced in historical simulations and maintained in warming climates (Fig. 4b). However, the connection between pseudo-PC1/2 and AR clusters weakens as the shifting phase of the first and second EOF modes in the future climate (Supplementary Figs. 8, 9).

Both the thermodynamical (moisture) and dynamical (wind) effects are important for AR changes in future climate, to extents that vary seasonally and geographically[30–32]. While the increasing background moisture may increase the intensity of AR events via the thermodynamical process, changes in the dynamical process may reduce the frequency of AR activity in some regions including the U.S. West Coast[33]. Previous literature shows that the precipitation efficiency of ARs may be reduced by the undermining surface wind due to the weakening of the equator-to-pole temperature gradient in the warming climate[34,35]. It is worth noting that the AR detection algorithm we applied here uses a relative threshold to capture the dynamical structure of ARs, and therefore not sensitive to the changes in the thermodynamical field. Although the restrictive AR detection algorithm can better capture the AR's connection to the dynamical field, one shortcoming emerges in the future projection assessment: the changes counts of ARs and

clusters remain small because of the increasing IVT threshold for AR with increasing warming levels (Supplementary Fig. 10d). The distribution of AR-related IVT uniformly increases (by 2–7%) with warming levels (Supplementary Fig. 10d), which means that moderate ARs in the current climate may not be identified as ARs in the future climate. With that, future ARs have higher ranks in the AR category due to the increased IVT (Fig. 4d). There is no consistent change in the spacing and the landfall durations at warming levels (Supplementary Fig. 10b, c). Future changes in AR cluster counts differ by density (Fig. 4c). While the number of clusters with a density below 0.6 decreases as temperature increases, a significant increase in clusters with a density over 0.6 is shown at +4 °C level.

Discussion

The recent disastrous nine AR series that hit California illuminates the urgency to advance the understanding of AR clusters so that prevention actions can be planned as such events could potentially have higher flood risks. In the current study, we show that the impacts of AR clusters vary by cluster density, i.e., the fraction of AR condition in a cluster. We investigate the connection between AR clusters and large-scale circulation patterns and show that the circulation variability can modulate the density of AR clusters. We analyze how AR clusters and their connection to circulations will change under warming climates. While the linkage of AR clusters to the first two dominant modes of 500 hPa geopotential height variability weakens with the warming climate, the third mode, which has the highest connection to high-density clusters, maintains.

The future changes in the connection between Z500 PCs and AR clusters reveal that as the warming level increases, the relation between predictor and predictand in the current climate may change, which may result in enhanced or diminished predictive power because the variability of the predictor also changes with warming climates. Therefore, when assessing the prediction of a feature in the future climate, it is also important to examine the future behavior of its predictors to achieve a comprehensive analysis of prediction skills.

One source of uncertainty in investigating AR cluster characteristics is cluster identification. The cluster identification results may change by a small fraction if a different bandwidth is chosen. For example, the start and end date of a cluster may change, or one landfall could be included in another cluster. The main purpose of the current study is to understand the characteristics of AR clusters and their interaction with large-scale circulation, instead of developing a technique to accurately lock the start and end day of AR clusters. Besides, we conducted sensitivity tests on cluster identification with different bandwidths, we reached consistent results so that the conclusions stand (not shown). Additionally, we compared the distribution of AR density between Mean Shift and other methods such as fixed window which divides the time into equal pieces of period, and moving window mean (Supplementary Fig. 11). Results suggested Mean Shift outperforms the other two by showing a higher range of cluster density (i.e., fewer non-AR days in a cluster), meaning that Mean Shift identifies clusters that contain the temporally-packed back-to-back ARs.

Another source of uncertainty is the detection uncertainty[36], which is addressed by including two other detection algorithms that are either permissive[27] or using an absolute threshold[37]. We find higher agreement among algorithms for higher-density clusters (Supplementary Figs. 12, 13). In particular, the Z500 patterns for dense clusters are similar among detection algorithms. We speculate that the selected sample size differs significantly among detection algorithms. The fraction of time steps with ARs detected by permissive algorithms is 2–3.5 times as much as a restrictive algorithm (more in Methods). The fraction continues to increase with warming levels as more time steps are identified when an absolute threshold is applied. A high fraction of time steps within AR clusters can potentially be problematic because the cluster characteristics and the associated key patterns will reflect the total mean, and the difference between dense and sparse clusters will converge to the variation of the mean.

Methods

Reanalysis and model simulations

The data used in this study is retrieved from the fifth generation of the European Centre for Medium-Range Weather Forecasts Interim Reanalysis (ERA5)[38]. The original temporal and spatial resolution is hourly in 0.25° latitude by 0.25° longitude grids. We conducted AR detection on 6-h averaged IVT data. The 500 hPa geopotential height and 850 hPa meridional and zonal winds are used to understand the circulation pattern associated with AR clusters. The focused period is October to April, from 1979-2023. The season for 2022-2023 only includes October 2022 to February 2023 because that is the available data at the time of the investigation.

To estimate the impact over land for landfalling ARs, we retrieved precipitation data from the Climate Prediction Center (CPC) Global Unified Gauge-Based Analysis of Daily Precipitation[39] data. The CPC precipitation data is with a spatial resolution of 0.5° latitude and 0.5° longitude global grids. We also used the National Centers for Environmental Prediction (NCEP) North American Regional Reanalysis (NARR) data to examine the changes in soil moisture saturation and runoff due to AR clusters. To address the uncertainty due to observational records[40], we analyze the Parameter-elevation Relationships on Independent Slopes Model (PRISM)[41] precipitation observations.

To validate the robustness of AR cluster characteristics and associated circulation pattern, we examine ARs in the two sets of model simulations. The first set is the Tier 2 output of the Atmospheric River Tracking Method Intercomparison Project (ARTMIP), which includes AR detection results from multiple AR detection algorithms on Coupled Model Intercomparison Project (CMIP) Phases 5[42] and 6[43] multi-model ensembles. We utilize model output from the historical simulations from 1970-2000 in both CMIP5 and CMIP6. In this study, we included the AR detection in nine CMIP5/6 outputs from the TECA detection algorithm.

The second set of model simulations is the National Center for Atmospheric Research (NCAR) Community Earth System Model Version 2 Large Ensemble Project (CESM2-LENS)[44]. In this study, we select 30 CESM2 ensembles in both historical and future simulations. The selected period in 1960-2000 in historical simulations. The future simulation is run under the global warming scenario of SSP370 with time spanning 2015-2100. We selected years in future simulation based on global warming levels for 1850–1900 climate: 2015–2019 (+1 °C), 2020–2024 (+1.5 °C), 2040–2044 (+2 °C), 2065–2069 (+3 °C), and 2085–2089 (+4 °C).

AR detection

We applied the Toolkit for Extreme Climate Analysis Bayesian AR Detector (TECA-BARD)[45] to detect binary masks of ARs from the IVT field. The TECA-BARD includes a set of "plausible" AR detectors sampled by a Bayesian framework, which can produce AR masks similar to manually identified ARs by experts. The output from AR detection is binary masks showing the spatial boundary of AR events. Detection uncertainty is one of the major sources of uncertainty in AR measures[46–49]. While TECA-BARD is one of the restrictive algorithms, we also included two algorithms that are permissive. One is developed by Guan and Waliser[27] (GW15), which applies a set of criteria including a relative threshold of 85% of the IVT climatology and other thresholds on geometric shape and transport direction. The other one is developed by Rutz, Steenburgh[37] (RSR14) which uses an absolute threshold (250 kg m^{-1} s^{-1}) on the IVT field.

The fraction of time steps containing landfalling ARs varies by algorithms: 16.1% for TECA-BARD, 35.3% for GW15, and 56.6% for RSR14, which suggests that the spacing between AR landfalls is much smaller in RSR14 compared to TECA-BARD. As a result, the fraction of selected time steps for AR clusters is 41.0% for TECA-BARD, 72.3% for GW15, and 85.2% for RSR14. When absolute threshold (RSR14) is applied to AR clusters at different warming levels, the number of landfall AR counts decreases because more time steps are identified as ARs so that multiple landfalls may merge into one event (Supplementary Fig. 14a). This is reflected by the continuous decrease in the spacing between AR landfalls (Supplementary Fig. 14b). While the number of clusters with a density

below 0.8 decreases, the number of highly dense clusters (density over 0.8) increases by 300% at +4 °C level (Supplementary Fig. 15a). However, for RSR14, the time steps within AR landfall and AR cluster are 64.5% and 89.1% at +4 °C level.

AR cluster identification—Mean Shift

Mean Shift is a general nonparametric technique to delineate arbitrarily shaped clusters, which is a fully data-driven unsupervised machine learning technique that has no physical process-based constraints. The Mean Shift algorithm aims to converge data points to the local maxima by iteratively performing the shift operation based on kernel density estimation[50,51]. The Mean Shift algorithm is implemented in the Python sklearn.cluster module. We used the Mean Shift Python module to conduct clustering of landfalling ARs over the U.S. West Coast. First, we calculated a 6-h time series of binary landfall flags with 0 s for no AR activity and 1 s for AR conditions over the U.S. West Coast. The determination of landfall is based on whether the instantaneous AR binary masks overlap with the land mask of the U.S. West Coast. During this step, the landfall activity of ARs and the landfall duration are all captured in the binary landfall flag. Next, we generate an index series that contains the time location index of 1 s in the binary landfall flags. The index series was the input data for Mean Shift. With the given bandwidth, the algorithm will automatically identify clusters of AR landfall days. The bandwidth is determined using the sklearn.cluster.estimate_bandwidth function which returns the estimated bandwidth to use with the mean-shift algorithm. For ERA5 reanalysis, the bandwidth is 8 days. For CMIP5, CMIP6, and CESM2-LENS, the bandwidths vary from 7 days to 9 days. We understand that the starting and ending time steps may shift for some clusters when different bandwidths are applied. However, results are not sensitive to small variations of bandwidths (not shown).

EOF analysis

The EOF analysis is a statistical technique used to analyze the dominant patterns of variability in a dataset. We conducted the EOF analysis on the 500 hPa geopotential height anomaly field. Latitude weighting was performed on the grid points before the EOF calculation. First, we construct the spatial covariance matrix of the field and perform an eigenvalue decomposition to obtain the eigenvalues and eigenvectors. The eigenvalues represent the amount of variance explained by each EOF mode, which are the principal components, while the eigenvectors represent the spatial patterns, which are the EOF modes.

Data availability

The ERA5 data can be downloaded at: https://cds.climate.copernicus.eu/cdsapp#!/dataset/reanalysis-era5-pressure-levels. Both CPC precipitation and NARR are provided by the NOAA PSL, Boulder, Colorado, USA, from their website at https://psl.noaa.gov. The PRISM Climate Data can be downloaded from https://prism.oregonstate.edu/. The ARTMIP Tier 2 dataset can be retrieved from https://www.earthsystemgrid.org/dataset/ucar.cgd.artmip.html. The CESM2-LENS can be retrieved from https://www.earthsystemgrid.org/dataset/ucar.cgd.cesm2le.output.html. Processed data including the AR landfall flags and large-scale fields are archived in https://zenodo.org/records/10892381.

References

1. Bateman, J. January 2023 was nation's 6th warmest on record—month marked by atmospheric rivers, numerous tornadoes. Available from: https://www.noaa.gov/news/january-2023-was-nations-6th-warmest-on-record (2023).
2. Leung, L. R. & Qian Y. Atmospheric rivers induced heavy precipitation and flooding in the western US simulated by the WRF regional climate model. *Geophys. Res. Lett.* **36**, L03820 (2009).
3. Henn, B. et al. Extreme runoff generation from atmospheric river-driven snowmelt during the 2017 Oroville dam spillways incident. *Geophys. Res. Lett.* **47**, e2020GL088189 (2020).
4. Cao, Q., Mehran, A., Ralph, F. M. & Lettenmaier, D. P. The role of hydrological initial conditions on atmospheric river floods in the Russian River basin. *J. Hydrometeorol.* **20**, 1667–1686 (2019).
5. Siirila-Woodburn, E. R. et al. The role of atmospheric rivers on groundwater: lessons learned from an extreme wet year. *Water Resources Research.* **59**, e2022WR033061 (2023).
6. Fish, M. A., Wilson, A. M. & Ralph, F. M. Atmospheric river families: definition and associated synoptic conditions. *J. Hydrometeorol.* **20**, 2091–2108 (2019).
7. Fish, M. A. et al. Large-scale environments of successive atmospheric river events leading to compound precipitation extremes in California. *J. Clim.* **35**, 1515–1536 (2022).
8. Slinskey, E. A. et al. Subseasonal clustering of atmospheric rivers over the western United States. *J. Geophys. Res. Atmos.* **128**, e2023JD038833 (2023).
9. O'Brien, T. A. et al. Increases in future AR count and size: Overview of the ARTMIP tier 2 CMIP5/6 experiment. *J. Geophys. Res. Atmos.* **127**, e2021JD036013 (2022).
10. Rhoades, A. M. et al. The shifting scales of western U.S. landfalling atmospheric rivers under climate change. *Geophys. Res. Lett.* **47**, e2020GL089096 (2020).
11. Singh, I., Dominguez, F., Demaria, E. & Walter, J. Extreme landfalling atmospheric river events in Arizona: possible future changes. *J. Geophys. Res. Atmos.* **123**, 7076–7097 (2018).
12. Bowers, C., Serafin K. A, Tseng K. C, & Baker J. W. Atmospheric river sequences as indicators of hydrologic hazard in historical reanalysis and GFDL SPEAR future climate projections. *Earth's Future* **11**, e2023EF003536 (2023).
13. Michaelis, A. C. et al. Atmospheric river precipitation enhanced by climate change: a case study of the storm that contributed to California's Oroville dam crisis. *Earth's Future.* **10**, e2021EF002537 (2022).
14. Patricola, C. M. et al. Future changes in extreme precipitation over the San Francisco Bay Area: dependence on atmospheric river and extratropical cyclone events. *Weather Clim. Extremes* **36**, 100440 (2022).
15. DeFlorio, M. J. et al. From California's extreme drought to major flooding: evaluating and synthesizing experimental seasonal and sub-seasonal forecasts of landfalling atmospheric rivers and extreme precipitation during winter 2022/23. *Bull. Am. Meteorol. Soc.* **105**, E84–E104 (2024).
16. Ralph, F. M. et al. A scale to characterize the strength and impacts of atmospheric rivers. *Bull. Am. Meteorol. Soc.* **100**, 269–290 (2019).
17. Mundhenk, B. D., Barnes, E. A. & Maloney, E. D. All-season climatology and variability of atmospheric river frequencies over the North Pacific. *J. Clim.* **29**, 4885–4903 (2016).
18. Huang, H. et al. Sources of subseasonal-to-seasonal predictability of atmospheric rivers and precipitation in the Western United States. *J. Geophys. Res. Atmos.* **126**, e2020JD034053 (2021).
19. Benedict, J. J., Clement, A. C. & Medeiros, B. Atmospheric blocking and other large-scale precursor patterns of landfalling atmospheric rivers in the North Pacific: a CESM2 study. *J. Geophys. Res. Atmos.* **124**, 11330–11353 (2019).
20. Guirguis, K. et al. Atmospheric rivers impacting Northern California and their modulation by a variable climate. *Clim. Dyn.* **52**, 6569–6583 (2019).
21. Tseng, K. C. et al. Are multiseasonal forecasts of atmospheric rivers possible? *Geophys. Res. Lett.* **48**, e2021GL094000 (2021).
22. Kim, H., Zhou Y, & Alexander M. A. Changes in atmospheric rivers and moisture transport over the Northeast Pacific and western North America in response to ENSO diversity. *Clim. Dyn.* **52**, 7375–7388 (2019).

23. Duchon, C. E. Lanczos filtering in one and two dimensions. *J. Appl. Meteorol. Climatol.* **18**, 1016–1022 (1979).

24. Wallace, J. M. & Gutzler, D. S. Teleconnections in the geopotential height field during the northern hemisphere winter. *Month. Weather Rev.* **109**, 784–812 (1981).

25. Bell, G. D. & Janowiak, J. E. Atmospheric circulation associated with the midwest floods of 1993. *Bull. Am. Meteorol. Soc.* **76**, 681–696 (1995).

26. Toride, K. & Hakim G. J. Influence of low-frequency PNA variability on MJO teleconnections to North American atmospheric river activity. *Geophys. Res. Lett.* **48**, e2021GL094078 (2021).

27. Guan, B. & Waliser, D. E. Detection of atmospheric rivers: evaluation and application of an algorithm for global studies. *J. Geophys. Res.Atmos.* **120**, 12514–12535 (2015).

28. Giamalaki, K. et al. Future intensification of extreme Aleutian low events and their climate impacts. *Sci. Rep.* **11**, 18395 (2021).

29. Gan, B. et al. On the response of the Aleutian low to greenhouse warming. *J. Clim.* **30**, 3907–3925 (2017).

30. Gao, Y. et al. Dynamical and thermodynamical modulations on future changes of landfalling atmospheric rivers over western North America. *Geophys. Res. Lett.* **42**, 7179–7186 (2015).

31. Lavers, D. A. et al. Future changes in atmospheric rivers and their implications for winter flooding in Britain. *Environ. Res. Lett.* **8**, 034010 (2013).

32. Mahoney, K. et al. An examination of an inland-penetrating atmospheric river flood event under potential future thermodynamic conditions. *J. Clim.* **31**, 6281–6297 (2018).

33. Payne, A. E. et al. Responses and impacts of atmospheric rivers to climate change. *Nat. Rev. Earth Environ.* **1**, 143–157 (2020).

34. Dettinger, M. D. Climate change, atmospheric rivers, and floods in California—a multimodel analysis of storm frequency and magnitude changes. *J. Am. Water Resour. Assoc.* **47**, 514–523 (2011).

35. Jain, S., Lall, U. & Mann, M. E. Seasonality and interannual variations of northern hemisphere temperature: equator-to-pole gradient and ocean–land contrast. *J.Clim.* **12**, 1086–1100 (1999).

36. Rutz, J. J. et al. The Atmospheric River Tracking Method Intercomparison Project (ARTMIP): quantifying uncertainties in atmospheric river climatology. *J. Geophys. Res. Atmos.* **124**, 13777–13802 (2019).

37. Rutz, J. J., Steenburgh, W. J. & Ralph, F. M. Climatological characteristics of atmospheric rivers and their inland penetration over the Western United States. *Month. Weather Rev.* **142**, 905–921 (2014).

38. Hersbach, H. et al. The ERA5 global reanalysis. *Q. J. R. Meteorol. Soc.* **146**, 1999–2049 (2020).

39. Xie, P. P. et al. A Gauge-based analysis of daily precipitation over East Asia. *J. Hydrometeorol.* **8**, 607–626 (2007).

40. Gibson, P. B. et al. Climate model evaluation in the presence of observational uncertainty: precipitation indices over the contiguous United States. *J. Hydrometeorol.* **20**, 1339–1357 (2019).

41. Daly, C. et al. Physiographically sensitive mapping of climatological temperature and precipitation across the conterminous United States. *Int. J. Climatol*. **28**, 2031–2064 (2008).

42. Taylor, K. E., Stouffer, R. J. & Meehl, G. A. An overview of CMIP5 and the experiment design. *Bull. Am. Meteorol. Soc.* **93**, 485–498 (2012).

43. Eyring, V. et al. Overview of the coupled model intercomparison project phase 6 (CMIP6) experimental design and organization. *Geosci. Model Dev.* **9**, 1937–1958 (2016).

44. Rodgers, K. B. et al. Ubiquity of human-induced changes in climate variability. *Earth Syst. Dynam. Discuss* **2021**, 1–22 (2021).

45. O'Brien, T. A. et al. Detection of atmospheric rivers with inline uncertainty quantification: TECA-BARD v1.0. *Geosci. Model Dev.* **13**, 6131–6148 (2020).

46. Shields, C. A. et al. Atmospheric River Tracking Method Intercomparison Project (ARTMIP): project goals and experimental design. *Geosci. Model Dev.* **11**, 2455–2474 (2018).

47. Lora, J. M., Shields C. A. & Rutz J. J. Consensus and disagreement in atmospheric river detection: ARTMIP global catalogues. *Geophys. Res. Lett.* **47**, e2020GL089302 (2020).

48. Zhou, Y. et al. Uncertainties in atmospheric river lifecycles by detection algorithms: climatology and variability. *J. Geophys. Res. Atmos.* **126**, e2020JD033711 (2021).

49. O'Brien, T. A. et al. Detection uncertainty matters for understanding atmospheric rivers. *Bull. Amer. Meteor. Soc.***101**, E790–E796 (2020).

50. Comaniciu, D. & Meer, P. Mean shift: a robust approach toward feature space analysis. *IEEE Trans. Pattern Anal. Mach. Intell.* **24**, 603–619 (2002).

51. Cheng, Y. Mean shift, mode seeking, and clustering. *IEEE Trans. Pattern Anal. Mach. Intell.* **17**, 790–799 (1995).

Acknowledgements

Author contributions

Conception of the work: Y.Z. and M.W. Atmospheric river event detection and cluster identification: Y.Z. Reanalysis and model data analysis: Y.Z. Paper writing: Y.Z. Paper editing and reviewing: Y.Z., M.W. and W.C. Figures: Y.Z. Acquiring funding and in-kind support: W.C.

Competing interests

The authors declare no competing interests.

Additional information

Supplementary information The online version contains supplementary material available at https://doi.org/10.1038/s43247-024-01368-w.

Correspondence and requests for materials should be addressed to Yang Zhou.

Peer review information *Communications Earth & Environment* thanks the anonymous reviewers for their contribution to the peer review of this work. Primary Handling Editor: Aliénor Lavergne. A peer review file is available.

Reprints and permissions information is available at http://www.nature.com/reprints

Publisher's note Springer Nature remains neutral with regard to jurisdictional claims in published maps and institutional affiliations.